nature materials

ARTICLES

https://doi.org/10.1038/s41563-022-01275-5

Deterministic switching of a perpendicularly polarized magnet using unconventional spin–orbit torques in WTe_2

I-Hsuan Kao[1], Ryan Muzzio[1], Hantao Zhang[2], Menglin Zhu[3], Jacob Gobbo[1], Sean Yuan[1], Daniel Weber[4,5], Rahul Rao[6], Jiahan Li[7], James H. Edgar[7], Joshua E. Goldberger[4], Jiaqiang Yan[8,9], David G. Mandrus[8,9], Jinwoo Hwang[3], Ran Cheng[2,10], Jyoti Katoch[1] and Simranjeet Singh[1] ✉

Spin–orbit torque (SOT)-driven deterministic control of the magnetic state of a ferromagnet with perpendicular magnetic anisotropy is key to next-generation spintronic applications including non-volatile, ultrafast and energy-efficient data-storage devices. However, field-free deterministic switching of perpendicular magnetization remains a challenge because it requires an out-of-plane antidamping torque, which is not allowed in conventional spin-source materials such as heavy metals and topological insulators due to the system's symmetry. The exploitation of low-crystal symmetries in emergent quantum materials offers a unique approach to achieve SOTs with unconventional forms. Here we report an experimental realization of field-free deterministic magnetic switching of a perpendicularly polarized van der Waals magnet employing an out-of-plane antidamping SOT generated in layered WTe_2, a quantum material with a low-symmetry crystal structure. Our numerical simulations suggest that the out-of-plane antidamping torque in WTe_2 is essential to explain the observed magnetization switching.

Spin–orbit torque (SOT) has emerged as an efficient means of manipulating the magnetic state of ferromagnetic (FM) materials[1–4]. The potential technological applications of SOT-driven magnetization manipulation include energy-efficient non-volatile magnetic memories[5] and spin–torque oscillators[6,7]. In SOT-induced magnetic switching, a charge-current density $\mathbf{j}_c$ (x direction) flowing in the plane of a bilayer structure consisting of spin-source material and a ferromagnet results in a spin current flowing in the out-of-plane direction (z direction) via spin galvanic effects[1–3]. This spin current in turn exerts a torque on the magnetization of a nearby magnetic layer. This torque has an antidamping component $\boldsymbol{\tau}_{\rm AD} \propto \hat{\mathbf{m}} \times \hat{\mathbf{p}} \times \hat{\mathbf{m}}$ and a field-like component $\boldsymbol{\tau}_{\rm FL} \propto \hat{\mathbf{p}} \times \hat{\mathbf{m}}$, where $\hat{\mathbf{m}}$ is the magnetization direction and $\hat{\mathbf{p}}$ is the spin polarization direction. Due to the symmetry of heavy-metal (HM)/FM bilayer heterostructures, the spin is polarized in the y direction and the in-plane antidamping torque ($\boldsymbol{\tau}_{\rm IP}^{\rm AD}$) has the form of $\hat{\mathbf{m}} \times \hat{\mathbf{y}} \times \hat{\mathbf{m}}$ and can only deterministically switch the magnetization of a magnet that has an in-plane magnetic anisotropy[3,8]. However, for memory applications, magnets with perpendicular magnetic anisotropy (PMA) are highly desired because this allows for ultra-compact packing and thermally stable, nanometre-sized magnetic bits[5]. In conventional HM/FM systems, an external magnetic field is applied along the direction of the charge current to break the in-plane symmetry of the system, allowing for deterministic switching of the magnetization state of a PMA magnet[1,3]. Previously, a structural asymmetry[9,10], tilted anisotropy of the nanomagnet[11], an in-plane magnetized layer[12–14], an in-plane effective magnetic field in FM/ferroelectric structures[15], anomalous Hall effect (AHE) and planar Hall effect in FM/HM/FM trilayers[16], and interplay of SOT and spin-transfer torque[17] have been explored to achieve a field-free deterministic switching of PMA magnets using SOTs. Another approach for this is to explore the utility of emergent quantum systems as a spin-source material wherein SOTs can be controlled by crystal symmetries. Recently, transition-metal dichalcogenides with low-symmetry crystal structures, such as WTe_2, have been shown to exhibit an out-of-plane antidamping torque ($\boldsymbol{\tau}_{\rm OP}^{\rm AD}$) of the form $\hat{\mathbf{m}} \times \hat{\mathbf{z}} \times \hat{\mathbf{m}}$ when a charge current is applied along the low-symmetry axis of the WTe_2/FM bilayer system[18,19]. In addition, an efficient field-free SOT switching, due to a strong charge-to-spin conversion efficiency in WTe_2, of an in-plane ferromagnet has been demonstrated in WTe_2/permalloy bilayer systems with a very small charge density ($\sim 2.96 \times 10^9\,{\rm A\,m^{-2}}$)[20]. However, it has not yet been established experimentally whether the unconventional out-of-plane antidamping SOT in layered materials with low-crystal symmetry is strong enough to enable the deterministic switching of a PMA magnet.

Here we experimentally realize field-free deterministic switching of a perpendicularly polarized magnet using SOTs in a quantum material with a low-symmetry crystal structure. For this, we fabricate SOT devices using a van der Waals-based layered quantum material platform. Thin films of WTe_2 are used as a spin-source material for generating SOTs[18,20–22]. In addition to the generation of

---

[1]Department of Physics, Carnegie Mellon University, Pittsburgh, PA, USA. [2]Department of Electrical and Computer Engineering, University of California Riverside, Riverside, CA, USA. [3]Department of Materials Science and Engineering, The Ohio State University, Columbus, OH, USA. [4]Department of Chemistry, The Ohio State University, Columbus, OH, USA. [5]Battery and Electrochemistry Laboratory (BELLA), Institute of Nanotechnology, Karlsruhe Institute of Technology, Eggenstein-Leopoldshafen, Germany. [6]Materials and Manufacturing Directorate, Air Force Research Laboratory, Wright-Patterson Air Force Base, Dayton, OH, USA. [7]Tim Taylor Department of Chemical Engineering, Kansas State University, Manhattan, KS, USA. [8]Materials Science and Technology Division, Oak Ridge National Laboratory, Oak Ridge, TN, USA. [9]Department of Materials Science and Engineering, The University of Tennessee, Knoxville, TN, USA. [10]Department of Physics and Astronomy, University of California Riverside, Riverside, CA, USA. ✉e-mail: simranjs@andrew.cmu.edu

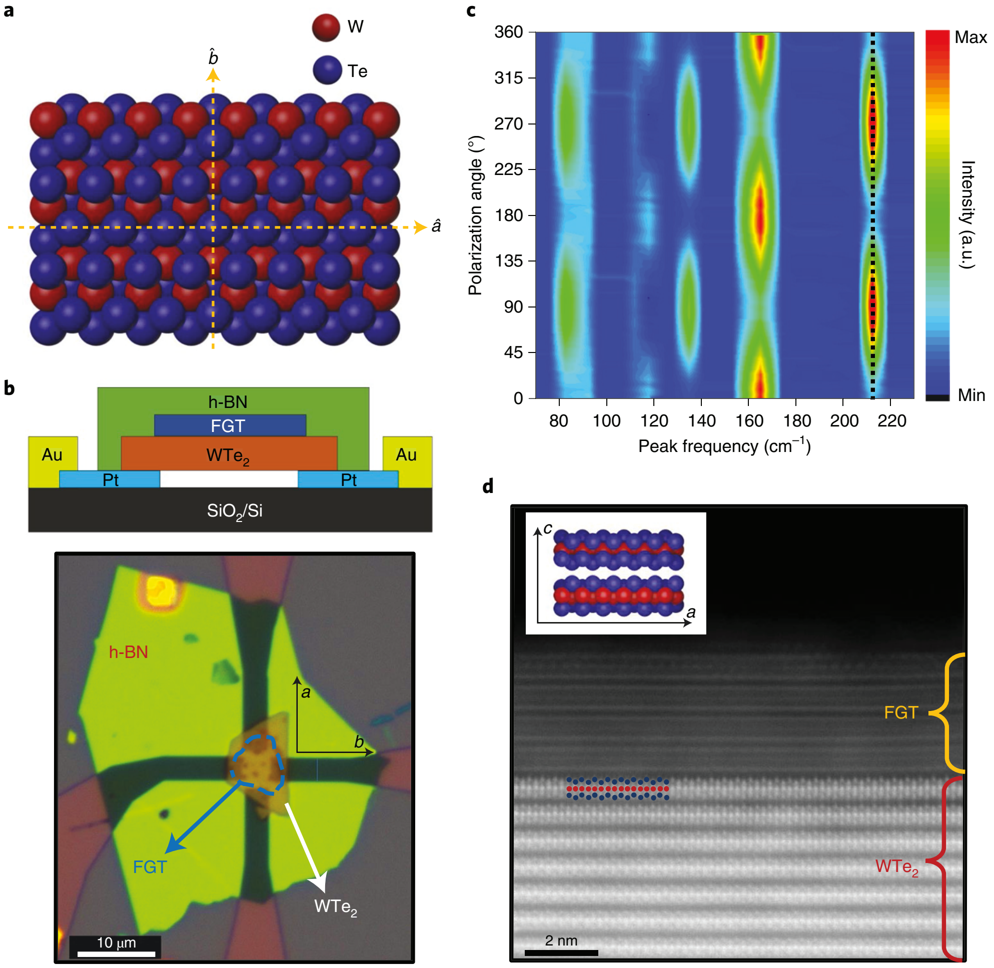

Fig. 1 | Crystal structure, polarized Raman and electron microscopy of the SOT devices. **a**, A model showing the crystal structure of WTe$_2$ with *a* and *b* axes labelled. The crystal is invariant (non-invariant) upon a *bc* (*ac*) mirror operation. **b**, Top: a schematic showing the side view of the device. Bottom: an optical image of device A. The electrodes are set up to allow the application of current pulses along the *a* and *b* axes of WTe$_2$. The FGT, WTe$_2$ and h-BN flakes are clearly labelled. **c**, The angle-dependent polarized Raman spectral intensity of a WTe$_2$ flake used in device A. The measurements were obtained by rotating the laser polarization with respect to the long edge (*a* axis) of the WTe$_2$ flake. The dashed line indicates the Raman peak at 212 cm^{-1} **d**, Cross-sectional STEM image of the device viewed along the *b*-axis orientation of WTe$_2$, confirming that the lateral direction is the *a* axis of WTe$_2$. Inset: the atomic arrangement in WTe$_2$ in the *ac* plane.

an out-of-plane antidamping torque, WTe$_2$ also exhibits properties that are highly relevant to achieving a large charge-to-spin conversion efficacy: strong spin–orbit coupling, non-trivial band dispersion, topologically protected spin-polarized bulk and surface states, a pronounced Edelstein effect and an intrinsic spin Hall effect[20–22]. WTe$_2$ is a low-symmetry system, the *ab* plane of which is schematically depicted in Fig. 1a (with the *c* axis normal to the *ab* plane). The surface of WTe$_2$ only has mirror symmetry with respect to the *bc* plane but not about the *ac* plane. Thus, the system is asymmetric relative to a 180° rotation about the *c* axis. For the PMA magnet, we utilize Fe$_{2.78}$GeTe$_2$ (FGT), which is a layered van der Waals FM material[23,24]. Mechanical dry-transfer techniques to assemble WTe$_2$/FGT bilayers and standard device fabrication techniques are used to prepare the SOT devices (Methods and Supplementary Note 1).

In total, we have measured six WTe$_2$/FGT devices and here we present data from devices A and F. The heterostructures of devices A and F consist of WTe$_2$ (25.8)/FGT (4.1)/h-BN (39.6) and WTe$_2$ (10.2)/FGT (9.0)/h-BN (31.3) respectively, where the numbers in parentheses indicate the layer thicknesses in nanometres and h-BN is hexagonal boron nitride. An optical micrograph of device A is shown in Fig. 1b along with a side-view schematic of the device (top panel). The crystallographic *a* and *b* axes are labelled in Fig. 1b, and are confirmed by polarized Raman spectroscopy[25]. Raman spectra are collected by rotating the polarization of the incident laser for different angles relative to the *a* axis of WTe$_2$ and the integrated intensities under each peak are calculated for the contour plot shown in Fig. 1c. The polarization angle dependence of the device A Raman peak at 212 cm^{-1} (corresponding to the black dashed line in Fig. 1c) exhibits minimum intensity when the excitation laser polarization is along the straight edge of the WTe$_2$ flake (Fig. 1b). This is consistent with previous reports[20,25] and clearly distinguishes the *a* axis of WTe$_2$. We have also carried out atomic structure characterization of device A using scanning transmission electron microscopy (STEM). Figure 1d shows an STEM cross-sectional image, confirming that the lateral direction is indeed the *a* axis of WTe$_2$, consistent with the orientation determined by the Raman spectra. The inset of Fig. 1d schematically shows the atomic arrangement of WTe$_2$ in the *ac* plane in comparison to the STEM image. We have confirmed the crystallographic orientation of WTe$_2$ in a total of five devices (including device F for which data are presented below) by polarized Raman spectroscopy and STEM (Supplementary Note 2).

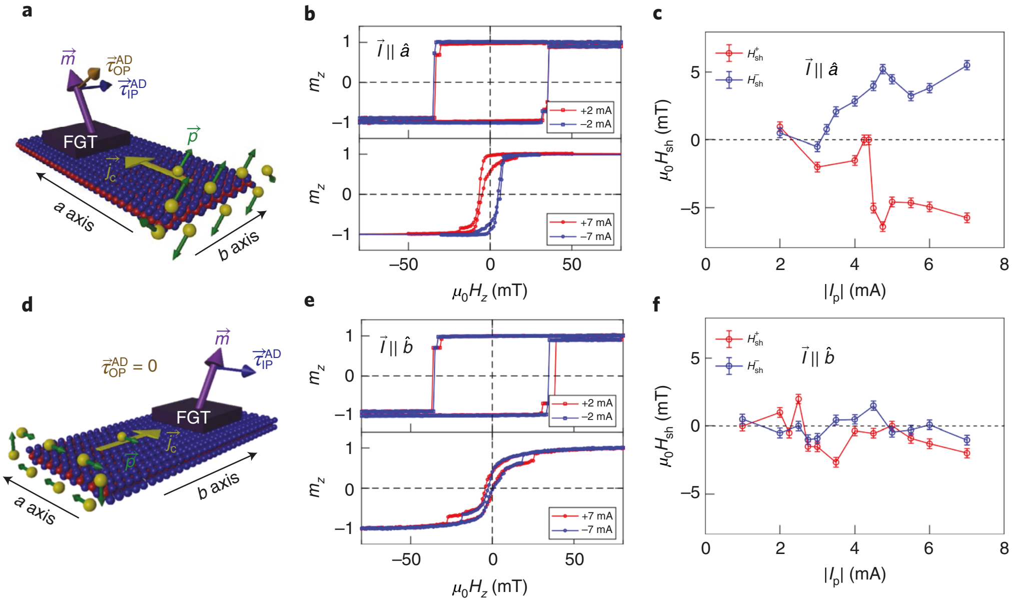

Fig. 2 | Current-induced AHE loop shift due to out-of-plane antidamping SOT in device A. a,**d**, A schematic showing the allowed forms of antidamping SOTs depending on whether a charge current is applied along the *a* axis (**a**) or *b* axis (**d**) of WTe_2. When a charge current is applied along the *a* axis, there is an out-of-plane component of the spin polarization as shown by green arrows in **a**. However, when a charge current is applied along the *b* axis, there is only an in-plane component of spin polarization as shown by green arrows in **d**. Thus, when a charge current is applied along the *a* axis (*b* axis), the out-of-plane antidamping torque has non-zero (zero) magnitude. **b**,**e**, The measured AHE hysteresis loops with $\mathbf{H} \parallel \hat{\mathbf{z}}$ while a charge current is applied along the *a* axis (**b**) or *b* axis (**e**). For a charge current applied along the *a* axis, the AHE loop shifts to negative (positive) fields for +7 mA (−7 mA) as shown in **b**. However, when a charge current is applied along the *b* axis, the AHE loops remain centred around zero field for both +7 mA and −7 mA (**e**). m_z, magnetization state. **c**,**f**, The loop shift field ($H^{\pm}_{sh}$) measured as a function of charge current amplitude $|I_p|$ for positive (H^{+}_{sh}) and negative (H^{-}_{sh}) charge current applied along the *a* axis (**c**) or *b* axis (**f**). The data are measured at 170 K. μ_0, magnetic permeability of free space.

The presence of a strong $\boldsymbol{\tau}^{AD}_{OP}$ in a WTe_2/permalloy heterostructure was previously probed by spin–torque ferromagnetic resonance[18]. The $\boldsymbol{\tau}^{AD}_{OP}$ is independent of the reversal of magnetization, reverses with current direction and can efficiently switch a perpendicular magnetization. The $\boldsymbol{\tau}^{AD}_{OP}$ is not allowed in conventional spin-source systems, such as HMs and topological insulators, due to two-fold rotational symmetry[18,19]. However, this symmetry is broken in WTe_2. Specifically, WTe_2 has no mirror symmetry in the *ac* plane (Fig. 1a), allowing for a non-zero $\boldsymbol{\tau}^{AD}_{OP}$ when a charge current is applied along its *a* axis (Fig. 2a)[18,19]. On the other hand, when a charge current is applied along the *b* axis of WTe_2, the preserved mirror symmetry in the *bc* plane requires that $\boldsymbol{\tau}^{AD}_{OP} = 0$ as depicted in Fig. 2d. Essentially, when a current is applied along the *b* axis and a *bc* plane mirror operation is performed, the current does not switch direction (that is, $I \rightarrow I$), but the out-of-plane antidamping torque (a pseudovector) will change sign (that is, $\boldsymbol{\tau}^{AD}_{OP} \rightarrow -\boldsymbol{\tau}^{AD}_{OP}$). But a current-induced torque must change sign with current reversal, requiring that $\boldsymbol{\tau}^{AD}_{OP} = 0$ when the current is along the *b* axis[18,19].

To examine the presence of $\boldsymbol{\tau}^{AD}_{OP}$, we perform AHE loop shift measurements (Methods). An $\boldsymbol{\tau}^{AD}_{OP}$ can abruptly shift the AHE hysteresis loop once the current passes a threshold value such that the intrinsic damping is compensated[1,16]. When a charge current pulse (I_p) is applied along the *a* axis (that is, $\mathbf{I} \parallel \hat{\mathbf{a}}$), AHE hysteresis loops measured at low pulse currents ($I_p = \pm 2$ mA) look identical for different current polarity as shown in the top panel of Fig. 2b. However, when I_p increases to +(−)7 mA (Fig. 2b, bottom), the AHE loop shifts to the negative (positive) field values. On the other hand, when I_p is applied along the *b* axis, no notable loop shift is observed for both low and high current pulse magnitudes (Fig. 2e). Note that there is also a reduction in the coercive field at high current densities that is mainly caused by Joule heating (Supplementary Note 5). The measurements are repeated at different charge current magnitudes for $\mathbf{I} \parallel \hat{\mathbf{a}}$ and $\mathbf{I} \parallel \hat{\mathbf{b}}$ and are shown in Fig. 2c,f, respectively. When $\mathbf{I} \parallel \hat{\mathbf{a}}$, we observe a threshold current effect in $H_{sh}(|I_p|)$ and a clear splitting between H^{+}_{sh} and H^{-}_{sh} at higher currents, where H^{+}_{sh} (H^{-}_{sh}) is the loop shift field measured at positive (negative) current. We speculate that the observed asymmetry in $H_{sh}(|I_p|)$ for positive and negative currents may be due to the fact that the device is not patterned into an ideal Hall cross-geometry. In contrast, for $\mathbf{I} \parallel \hat{\mathbf{b}}$, $H_{sh}(|I_p|)$ shows very weak I_p dependence and remains close to zero for low and high current values, which is similar to what has been reported previously for conventional HM/FM systems[1]. These results clearly show the presence of a non-zero $\boldsymbol{\tau}^{AD}_{OP}$ when current is applied along the *a* axis. The abrupt shift, instead of a linear shift, in H_{sh} for $\mathbf{I} \parallel \hat{\mathbf{a}}$ also indicates that no significant out-of-plane field-like torque is present in the system[9].

Next, we demonstrate field-free switching of perpendicular magnetization of FGT employing charge-current-induced SOTs in WTe_2 (see Methods for measurement details). When $\mathbf{I} \parallel \hat{\mathbf{a}}$, we observe a clear deterministic switching (Fig. 3a). Figure 3a shows that the terminal state is determined by the polarity of I_p, that is, a positive current favours magnetization pointing up and a negative current favours magnetization pointing down. We attribute the observed deterministic switching of FGT to $\boldsymbol{\tau}^{AD}_{OP}$ generated by the out-of-plane spin polarization, p_z, injected from WTe_2.

On the other hand, the behaviour is completely different when the current is applied along the *b* axis. There is no deterministic switching observed in the absence of an external in-plane magnetic field (Fig. 3b). This behaviour is similar to SOT switching in conventional HM/FM bilayer systems, that is, the terminal state is close to the demagnetized state $m_z \approx 0$, indicating that $\boldsymbol{\tau}^{AD}_{IP}$, generated by spin polarization pointing in the *y* direction, drives the magnetic moment of FGT to the device plane[1]. Without the presence of p_z (or a symmetry-breaking in-plane magnetic field), multidomains

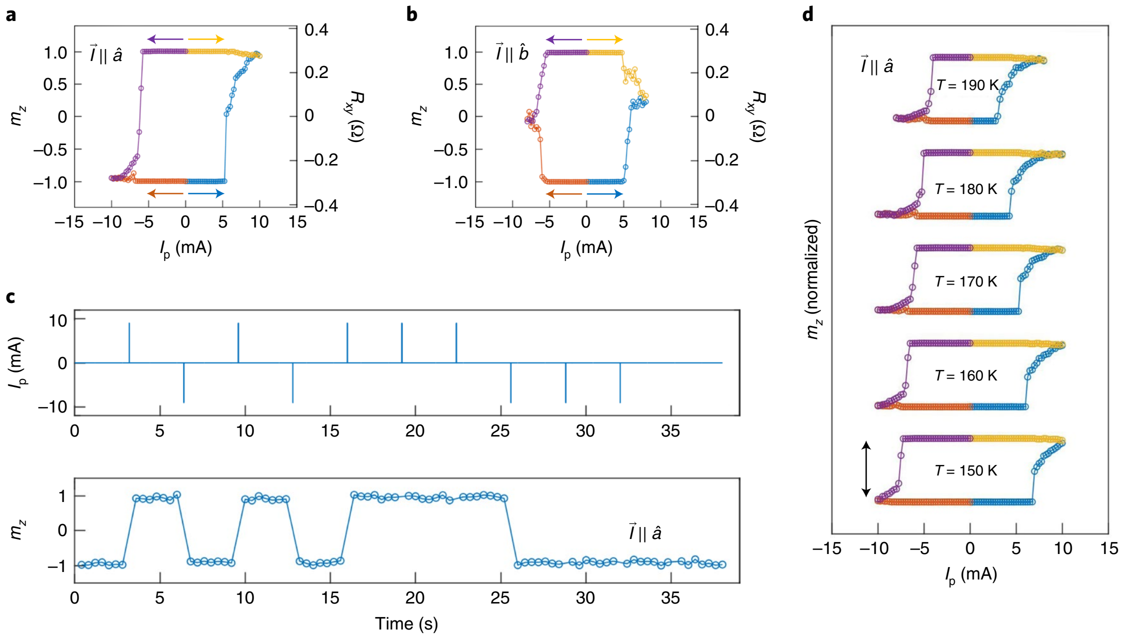

Fig. 3 | SOT-induced-field-free switching in WTe$_2$/ FGT bilayers (device A). a,b, The magnetization state of FGT is initialized to $m_z = -1$ (blue and orange data) or $m_z = +1$ (yellow and purple data). Then the magnitude of the current pulse is increased gradually from zero with the direction of the current indicated by the arrows, while the FGT magnetization state is detected by AHE. When **I** ∥ **â** (**a**), we see a clear deterministic switching from $m_z = -1$ to $m_z = +1$ only when a positive charge current is applied (switching happens at approximately +6 mA). On the other hand, a negative current (approximately −6 mA) switches it from $m_z = +1$ to $m_z = -1$. This is indeed consistent with magnetic switching due to $\boldsymbol{\tau}_{\mathrm{OP}}^{\mathrm{AD}}$ because the final state is determined by the polarity of the charge current. Note that in **a** we did not apply any symmetry-breaking in-plane magnetic field to induce the observed deterministic SOT switching. However, for the case when a charge current is applied along the *b* axis, we do not observe a deterministic switching (**b**) in the absence of an in-plane magnetic field. These observations are consistent with presence (absence) of $\boldsymbol{\tau}_{\mathrm{OP}}^{\mathrm{AD}}$ when a charge current is applied along the *a* axis (*b* axis). **c**, Deterministic switching by a series of 500 μs current pulses applied along the *a* axis. The magnitude of the write pulse is 9 mA, corresponding to $J = 9.8 \times 10^{10}$ A m^{-2}. **d**, Current-induced SOT switching while **I** ∥ **â** performed at various temperatures. The black arrow shows the difference between $m_z = -1$ and $m_z = +1$.

are formed after the current is turned off. Each domain is then left randomly oriented which leads to the demagnetization of FGT. Furthermore, using a train of positive and negative current pulses applied along the *a* axis of WTe$_2$ (Fig. 3c, top) we can reliably and deterministically switch the magnetic state of the FGT from up to down and vice versa (Fig. 3c, bottom). In addition, the field-free SOT switching of FGT magnetization is robust in a wider temperature range as shown in Fig. 3d. We did not perform the switching experiments below 150 K to avoid potential device damage at the high current densities that are required to achieve the switching because of the increasing coercive field of FGT (Supplementary Note 4).

The thermal effect due to Joule heating in our devices is estimated by comparing the temperature and charge-current-dependent longitudinal resistance of the WTe$_2$/FGT bilayer (Supplementary Note 5). For this, we look at a device F in which we have thinner WTe$_2$ (higher resistance), such that a larger current flows through the FGT layer giving us a more accurate estimation of the temperature profile of magnetic layer due to Joule heating (Supplementary Note 3). The threshold current (I_{th}), defined as the current that switches the magnetic state across $m_z = 0$, is obtained at different temperatures and translated to the threshold current density (J_{th}), considering only current flowing in WTe$_2$ for both the *a* axis and the *b* axis (Fig. 4a). The inset of Fig. 4a shows the field-free SOT switching observed in device F when a charge current is applied along the *a* axis. We also estimate ΔT, which is the change in temperature of the device when the I_{th} current pulse is applied. We observe that ΔT is higher (lower) when we perform SOT-switching experiments at lower (higher) temperatures. At lower temperatures, FGT coercive fields are higher (Supplementary Note 4) and will require larger Joule heating (a larger ΔT value) and hence large current densities to switch the magnetization as observed in Fig. 4b. These results suggest that Joule heating assists the SOT-induced magnetization reversal by lowering the energy barrier for magnetization switching in our low-temperature SOT-switching experiments. In addition, it is clear from Fig. 4b that the temperature of the device remains below the Curie temperature (T_c). The red dashed line in Fig. 4b indicates the ΔT that is required to surpass the T_c when switching experiments are performed at various temperatures (140–200 K).

To better distinguish the roles of $\boldsymbol{\tau}_{\mathrm{IP}}^{\mathrm{AD}}$ and $\boldsymbol{\tau}_{\mathrm{OP}}^{\mathrm{AD}}$, we perform numerical simulations of magnetization switching for a monodomain FGT. While the actual switching processes are likely to involve domain-wall motions, it is customary to use a monodomain simulation that captures the essential physics behind the switching process[26,27], which is simple enough for an intuitive understanding. To this end, we use the coercive field as the effective anisotropy[3]. We also take thermal effects into account by considering the temperature dependence of the coercive field in the presence of current-induced Joule heating (Supplementary Notes 4 and 5), which yields the effective anisotropy in our simulations as a function of the applied current and the setting temperature. We first investigate the case of **I** ∥ $\hat{\mathbf{b}}$ at 160 K. As shown in Fig. 4c, by varying the current density in WTe$_2$ (j_c) and the ratio of $\boldsymbol{\tau}_{\mathrm{IP}}^{\mathrm{AD}}/j_c$, we find that the initial state ($m_z = -1$) can be switched to an in-plane direction ($m_z = 0$) that is energetically metastable. The threshold decreases with an increasing $\boldsymbol{\tau}_{\mathrm{IP}}^{\mathrm{AD}}/j_c$ as reflected by the phase boundary. If the driving current is turned off, the metastable state ($m_z = 0$) will equally probably relax towards $m_z = -1$ and $m_z = 1$. In reality, the metastable state will

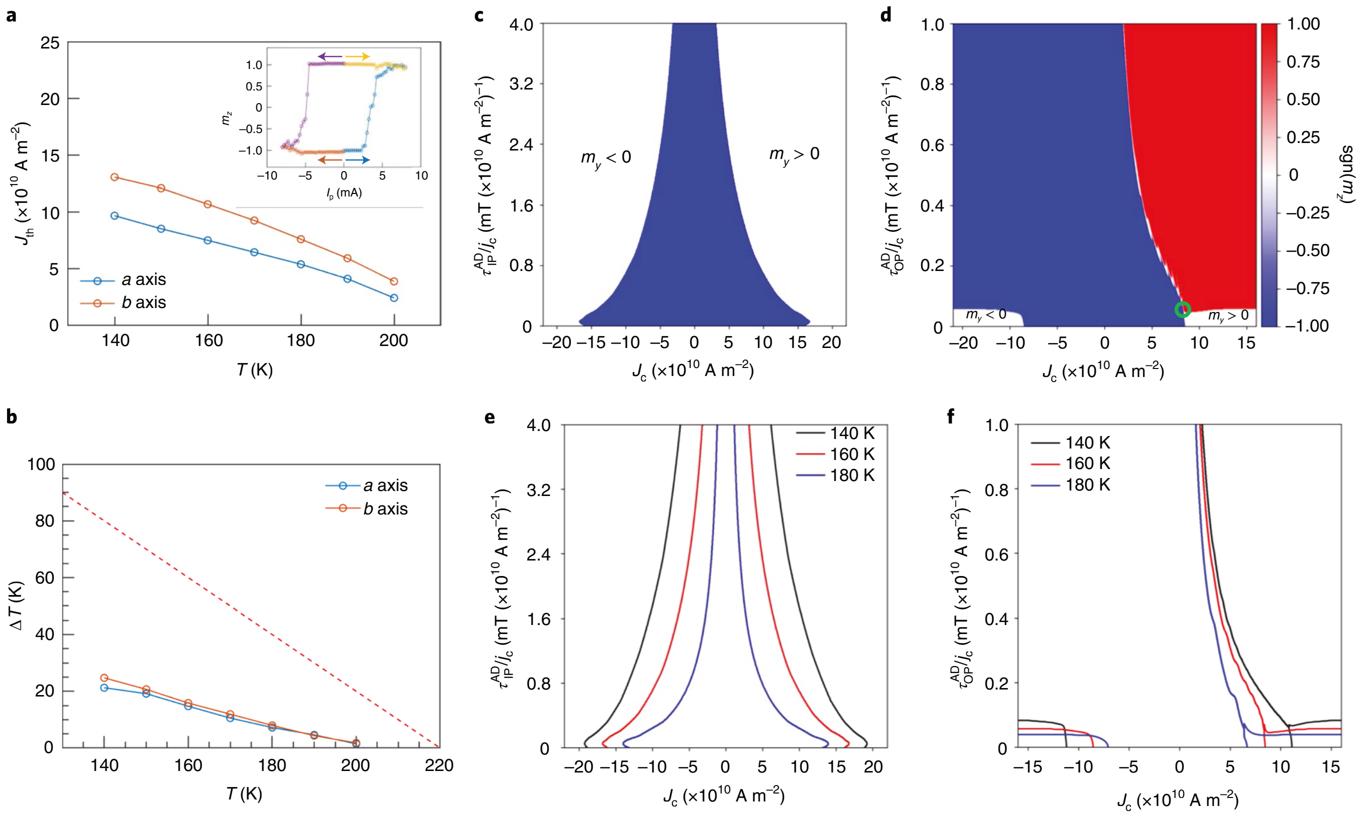

Fig. 4 | Simulation of SOT-induced switching, Joule heating and temperature dependences. **a**, The threshold current density J_{th} as a function of temperature obtained for a charge current applied along the *a* and *b* axes for device F. For both cases, a larger J_{th} is required to switch the magnetization of FGT at lower temperatures. Inset: SOT-induced-field-free deterministic switching for $\mathbf{I} \parallel \hat{\mathbf{a}}$ at 160 K. **b**, The temperature rise, Δ*T*, from the setting temperature (that is, the temperature at which switching experiments is performed) ascribed to Joule heating (when J_{th} is reached) for a charge current applied along the *a* and *b* axes. At lower temperatures, Δ*T* is higher, suggesting a larger Joule heating (and hence a higher current density) is associated with the switching process. The red dashed line depicts the Δ*T* that is required to exceed the T_c at different temperatures where switching experiments are performed. **c**,**d**, Simulations for monodomain magnetization switching when a charge current is applied along the *b* axis (**c**) or *a* axis (**d**) at 160 K. The initial magnetic state is set to be $m_z=-1$, and the blue, red and white regions correspond to unswitched, switched ($m_z=1$) and metastable ($m_z=0$) states, respectively. When a current is applied along the *b* axis (**c**), $\boldsymbol{\tau}_{IP}^{AD}$ switches the magnetization to a metastable state with $m_z=0$ and $m_y>0$ ($m_y<0$) for positive (negative) current. When a charge current is applied along the *a* axis (**d**), an out-of-plane antidamping torque $\boldsymbol{\tau}_{OP}^{AD}$ is generated, and the magnetization can only be switched for a positive current direction. If $\boldsymbol{\tau}_{OP}^{AD}$ is not strong enough, however, $\boldsymbol{\tau}_{IP}^{AD}$ will dominate and switch the magnetization only to the metastable magnetic states, that is, no deterministic switching occurs. **e**,**f**, The phase boundaries at various temperatures for FGT monodomain switching for a charge current applied along the *b* axis (**e**) or *a* axis (**f**). The $\boldsymbol{\tau}_{IP}^{AD}/j_c$ used at 140, 160 and 180 K is 0.86, 0.59 and 0.41 mT (×10^{10} A m^{-2})$^{-1}$, respectively, in **f**. The threshold current density becomes larger at lower temperatures, consistent with the experimental results in **a**.

easily break up into multiple domains with an average $\langle m_z \rangle = 0$. This is consistent with Fig. 3b, justifying that an in-plane torque $\boldsymbol{\tau}_{IP}^{AD}$ alone is unable to switch the magnetization from $m_z=-1$ to $m_z=1$. Using the threshold J_{th} for the *b* axis at $T=160\,K$ read off from Fig. 4a, we can evaluate in Fig. 4c the value of $\boldsymbol{\tau}_{IP}^{AD}/j_c$. We emphasize that in the effective monodomain picture, this value does not have quantitative correspondence but only serves as an intermediate quantity in the simulation. With this $\boldsymbol{\tau}_{IP}^{AD}/j_c$, we can then simulate the switching process for $\mathbf{I} \parallel \hat{\mathbf{a}}$ by varying j_c and $\boldsymbol{\tau}_{OP}^{AD}/j_c$ at 160 K. As shown in Fig. 4d, we find three different phases characterized by the final state of m_z: the unswitched phase ($m_z=-1$), the switched phase ($m_z=1$) and the in-plane metastable phase ($m_z=0$). These phases intersect at a tricritical point (Fig. 4d, green circle), which does not exist when j_c flips sign. It is clear from Fig. 4d that the switched phase only exists when the ratio of $\boldsymbol{\tau}_{OP}^{AD}/j_c$ is above the tricritical point, and the phase boundary of magnetization switching continuously shifts towards smaller j_c. This striking feature strongly indicates that the out-of-plane antidamping torque $\boldsymbol{\tau}_{OP}^{AD}$ is essential for the magnetization switching in the perpendicular direction, consistent with the earlier micromagnetic simulations that consider both $\boldsymbol{\tau}_{IP}^{AD}$ and $\boldsymbol{\tau}_{OP}^{AD}$ (ref. [28]). As a comparison, we also simulate the switching processes at 140 and 180 K and plot the phase boundaries along with that for 160 K in Fig. 4e,f, where we see that the threshold current for magnetization switching becomes larger (smaller) at lower (higher) temperatures, agreeing qualitatively with the observation in Fig. 4a. This behaviour is physically reasonable because at lower temperatures, the coercive field (which we adopt as the effective anisotropy) becomes larger so that the energy barrier for switching becomes higher. These results qualitatively explain the observed SOT switching in WTe$_2$/FGT bilayers by showing that $\boldsymbol{\tau}_{IP}^{AD}$ and $\boldsymbol{\tau}_{OP}^{AD}$ coexist, and in particular, that $\boldsymbol{\tau}_{OP}^{AD}$ needs to be large enough to achieve field-free deterministic switching as the terminal state will otherwise be demagnetized from the metastable phases.

We have experimentally demonstrated that an out-of-plane antidamping SOT in WTe$_2$ is strong enough to enable thermally assisted field-free magnetization switching of a magnet with PMA. The result from monodomain simulation excludes the possibility of deterministic switching without a strong enough out-of-plane antidamping SOT. There are still open questions that need to be addressed in the future, including the exact mechanism of magnetization switching observed in our devices, more comprehensive understanding of thermal effects on SOT switching, and the potential of realizing WTe_2-based scalable and room temperature functional SOT switching devices. However, the presence of a strong out-of-plane antidamping torque enabled by the special crystal symmetry in WTe_2 and its unique physical consequences make transition metal dichalcogenides with lower-symmetry crystal structure an appealing spin-source material for future SOT-related magnetic memory technologies.

Online content

Any methods, additional references, Nature Research reporting summaries, source data, extended data, supplementary information, acknowledgements, peer review information; details of author contributions and competing interests; and statements of data and code availability are available at https://doi.org/10.1038/s41563-022-01275-5.

Received: 26 October 2020; Accepted: 3 May 2022;
Published online: 16 June 2022

References

1. Miron, I. M. et al. Perpendicular switching of a single ferromagnetic layer induced by in-plane current injection. *Nature* **476**, 189–193 (2011).
2. Liu, L. et al. Spin–torque switching with the giant spin Hall effect of tantalum. *Science* **336**, 555–558 (2012).
3. Liu, L. et al. Current-induced switching of perpendicularly magnetized magnetic layers using spin torque from the spin Hall effect. *Phys. Rev. Lett.* **109**, 096602 (2012).
4. Mellnik, A. R. et al. Spin-transfer torque generated by a topological insulator. *Nature* **511**, 449–451 (2014).
5. Brataas, A. et al. Current-induced torques in magnetic materials. *Nat. Mater.* **11**, 372–381 (2012).
6. Liu, R. H. et al. Spectral characteristics of the microwave emission by the spin Hall nano-oscillator. *Phys. Rev. Lett.* **110**, 147601 (2013).
7. Cheng, R. et al. Terahertz antiferromagnetic spin Hall nano-oscillator. *Phys. Rev. Lett.* **116**, 207603 (2016).
8. Garello, K. et al. Symmetry and magnitude of spin–orbit torques in ferromagnetic heterostructures. *Nat. Nanotechnol.* **8**, 587–593 (2013).
9. Yu, G. et al. Switching of perpendicular magnetization by spin–orbit torques in the absence of external magnetic fields. *Nat. Nanotechnol.* **9**, 548–554 (2014).
10. Chen, S. et al. Free field electric switching of perpendicularly magnetized thin film by spin current gradient. *ACS Appl. Mater. Interfaces* **11**, 30446–30452 (2019).
11. You, L. et al. Switching of perpendicularly polarized nanomagnets with spin orbit torque without an external magnetic field by engineering a tilted anisotropy. *Proc. Natl Acad. Sci. USA* **112**, 10310–10315 (2015).
12. Lau, Y.-C. et al. Spin–orbit torque switching without an external field using interlayer exchange coupling. *Nat. Nanotechnol.* **11**, 758–762 (2016).
13. Fukami, S. et al. Magnetization switching by spin–orbit torque in an antiferromagnet–ferromagnet bilayer system. *Nat. Mater.* **15**, 535–541 (2016).
14. Oh, Y.-W. et al. Field-free switching of perpendicular magnetization through spin–orbit torque in antiferromagnet/ferromagnet/oxide structures. *Nat. Nanotechnol.* **11**, 878–884 (2016).
15. Cai, K. et al. Electric field control of deterministic current-induced magnetization switching in a hybrid ferromagnetic/ferroelectric structure. *Nat. Mater.* **16**, 712–716 (2017).
16. Baek, S.-h. C. et al. Spin currents and spin-orbit torques in ferromagnetic trilayers. *Nat. Mater.* **17**, 509–513 (2018).
17. Wang, M. et al. Field-free switching of a perpendicular magnetic tunnel junction through the interplay of spin–orbit and spin-transfer torques. *Nat. Electron.* **1**, 582–588 (2018).
18. MacNeill, D. et al. Control of spin–orbit torques through crystal symmetry in WTe_2/ferromagnet bilayers. *Nat. Phys.* **13**, 300–305 (2017).
19. Xue, F. et al. Unconventional spin–orbit torque in transition metal dichalcogenide–ferromagnet bilayers from first-principles calculations. *Phys. Rev. B* **102**, 014401 (2020).
20. Shi, S. et al. All-electric magnetization switching and Dzyaloshinskii–Moriya interaction in WTe_2/ferromagnet heterostructures. *Nat. Nanotechnol.* **14**, 945–949 (2019).
21. Feng, B. et al. Spin texture in type-II Weyl semimetal WTe_2. *Phys. Rev. B* **94**, 195134 (2016).
22. Johansson, A. et al. Edelstein effect in Weyl semimetals. *Phys. Rev. B* **97**, 085417 (2018).
23. Fei, Z. et al. Two-dimensional itinerant ferromagnetism in atomically thin Fe_3GeTe_2. *Nat. Mater.* **17**, 778–782 (2018).
24. Weber, D. et al. Decomposition-induced room-temperature magnetism of the Na-intercalated layered ferromagnet $Fe_{3-x}GeTe_2$. *Nano Lett.* **19**, 5031–5035 (2019).
25. Song, Q. et al. The polarization-dependent anisotropic Raman response of few-layer and bulk WTe_2 under different excitation wavelengths. *RSC Adv.* **6**, 103830–103837 (2016).
26. Chen, X. Z. et al. Antidamping-torque-induced switching in biaxial antiferromagnetic insulators. *Phys. Rev. Lett.* **120**, 207204 (2018).
27. Chen, X. et al. Electric field control of Néel spin–orbit torque in an antiferromagnet. *Nat. Mater.* **18**, 931–935 (2019).
28. Liao, Y.-C. et al. Spin-orbit-torque material exploration for maximum array-level read/write performance. *Tech. Dig. Int. Electron Devices Meet.* https://doi.org/10.1109/IEDM13553.2020.9371979 (2020).

Methods

Device fabrication. WTe_2, FGT and h-BN crystal flakes were prepared by previously published procedures[24,29,30]. WTe_2, h-BN and FGT were mechanically exfoliated on separate Si/SiO_2(300 nm) substrates inside an argon-filled glovebox. The flakes were then optically inspected and selected using a fully automated microscope inside the glovebox. On a separate substrate, electrodes were defined using standard electron beam lithography with methyl methacrylate/poly(methyl methacrylate) bilayer resist; electron beam deposition was used for the platinum electrodes. The heterostructure was made with a custom-built transfer tool inside the glovebox using a polydimethylsiloxane stamp and thin film of polycarbonate. The final device consists, from top to bottom, of h-BN/FGT/WTe_2/Pt with Cr(5 nm)/Au(110 nm) bond pads.

SOT measurements. The electrical measurements were performed at variable temperatures in high vacuum ($<10^{-5}$ mtorr) conditions. An electromagnet was rotated such that the magnetic field can be applied in both in- and out-of-plane directions of the device. A Keithley 6221 current source and a Keithley 2182A nanovoltmeter are used for AHE hysteresis loop and current pulse-induced SOT-switching experiments. The current pulse used is a square current pulse with varying magnitude and a width of 100 µs (unless stated otherwise). The transverse resistance, R_{xy}, is measured with a smaller-magnitude current (50 µA) in delta mode (unless stated otherwise) to determine the magnetization state of the FGT. We define the normalized perpendicular magnetization $m_z = \frac{M_z}{M_s} = \frac{R_{xy}}{R_{\mathrm{AHE}}}$, where M_z is the perpendicular magnetization and M_s is the saturation magnetization. In the SOT measurements, the initial magnetic state is prepared in $m_z = \pm 1$ (using an external magnetic field) and I_p is swept from zero to positive (negative) maximum values in steps of 250 µA. We define the threshold current $I_{\mathrm{th}} = (I_{\mathrm{th}}^{+} + I_{\mathrm{th}}^{-})/2$, where I_{th}^{+} (I_{th}^{-}) is the pulse current magnitude that drives the magnetization state across $m_z = 0$ at positive (negative) pulse sides. For SOT switching with pulse trains, a series of read current pulses of 500 µA were applied to read the magnetization state before and after the write current pulse was applied. AHE loop shift measurements are performed by measuring $m_z(H_z)$, where at each perpendicular field H_z a pulse current I_p (500 µs long) is applied and m_z is measured simultaneously in pulse delta mode. We define the loop shift field of the loop by $H_{\mathrm{sh}} = [H_c^{+} + H_c^{-}]/2$, where H_c^{+} (H_c^{-}) is the magnetic field for which the magnetization switches from down to up (up to down).

Numerical simulations. The effective single-domain dynamics is simulated by solving the Landau–Lifshitz–Gilbert equation in the presence of in-plane and out-of-plane antidamping torques as

$$\frac{\mathrm{d}\mathbf{m}}{\mathrm{d}t} = -\gamma H_{\mathrm{A}}(j_{\mathrm{c}}, T)\mathbf{m} \times m_z\widehat{\mathbf{z}} + c_{\mathrm{oe}} j_{\mathrm{c}}\widehat{\mathbf{x}} \times \mathbf{m} + \mathbf{m} \times \left[\left(c_{\mathrm{IP}}^{\mathrm{AD}} j_{\mathrm{c}}\widehat{\mathbf{y}} + c_{\mathrm{OP}}^{\mathrm{AD}} j_{\mathrm{c}}\hat{\mathbf{z}}\right) \times \mathbf{m}\right]$$
$$+ c_{\mathrm{OP}}^{\mathrm{FL}} j_{\mathrm{c}}\widehat{\mathbf{z}} \times \mathbf{m} + \alpha\mathbf{m} \times \frac{\mathrm{d}\mathbf{m}}{\mathrm{d}t}$$

where **m** is the unit vector of magnetization of FGT, t is time, H_{A} is the effective easy-axis anisotropy (taken as the coercive field, $H_{\mathrm{A}} = H_{\mathrm{c}}$), j_c is the charge current density, c_{oe}, $c_{\mathrm{IP}}^{\mathrm{AD}}$, $c_{\mathrm{OP}}^{\mathrm{AD}}$ and $c_{\mathrm{OP}}^{\mathrm{FL}}$ are the amplitudes of the Oersted field, the in-plane antidamping torque, the out-of-plane antidamping torque and the out-of-plane field-like torque with respect to j_c, respectively, and α is the Gilbert damping parameter. To incorporate the heating effects, we determine the dependences of the coercive field on the current and the setting temperature from the hysteresis loop and the resistance measurements (Supplementary Notes 4 and 5). Based on the materials parameters and the device geometry, we take and set $c_{\mathrm{oe}} = 6.4 \times 10^{-2}$ mT ($\times 10^{10}$ A m^{-2})$^{-1}$, $\alpha = 0.005$. In the simulations, we use $c_{\mathrm{OP}}^{\mathrm{FL}} = 0.5 c_{\mathrm{OP}}^{\mathrm{AD}}$, but we find that $c_{\mathrm{OP}}^{\mathrm{FL}}$ has negligible impact on the switching process; the result does not show visible differences if $c_{\mathrm{OP}}^{\mathrm{FL}} = 0$ or $c_{\mathrm{OP}}^{\mathrm{FL}} = 4 c_{\mathrm{OP}}^{\mathrm{AD}}$. The current density j_c is applied along the $\widehat{\mathbf{x}}$ direction, so the in-plane spin accumulation and the Oersted field are along the $\hat{\mathbf{y}}$ direction. The initial state of **m** is set to be along the $-\hat{\mathbf{z}}$ direction while including a negligibly small deviation to reduce the incubation time, and the final state is obtained when the system reaches equilibrium.

Data availability

All the data supporting the findings of this study are available in the article and its Supplementary Information. Further information is available from the corresponding author on reasonable request.

References

29. Zhao, Y. et al. Anisotropic magnetotransport and exotic longitudinal linear magnetoresistance in WTe_2 crystals. *Phys. Rev. B* **92**, 041104 (2015).
30. Liu, S. et al. Single crystal growth of millimeter-sized monoisotopic hexagonal boron nitride. *Chem. Mater.* **30**, 6222–6225 (2018).

Acknowledgements

Funding for this research was provided primarily by the Center for Emergent Materials at The Ohio State University, a National Science Foundation (NSF) MRSEC through award number DMR-2011876. R.M. acknowledges NSF support through an AGEP-GRS supplement to award DMR-1809145. H.Z. and R.C. are supported by the Air Force Office of Scientific Research under grant FA9550-19-1-0307. J.Y. acknowledges support from the US Department of Energy, Office of Science, Basic Energy Sciences, Materials Sciences and Engineering Division. D.G.M. acknowledges support from the Gordon and Betty Moore Foundation's EPiQS Initiative through grant number GBMF9069. J.E.G. acknowledges financial support from the Center of Emergent Materials, an NSF MRSEC, under grant number DMR-2011876. D.W. gratefully acknowledges the financial support by the German Science Foundation DFG Research Fellowship (WE6480/1). Support for h-BN crystal growth from the Office of Naval Research from award N00014-20-1-2427 is appreciated. Electron microscopy was performed at the Center for Electron Microscopy and Analysis at The Ohio State University.

Author contributions

S.S. and J.K. designed the experiments and supervised the research. I.-H.K., R.M., S.Y. and J.G. prepared the devices and performed the experiments. H.Z. and R.C. performed the numerical simulations. M.Z and J.H. performed the STEM measurements. R.R. carried out polarized Raman measurements. J.Y. and D.G.M. provided the bulk crystals of WTe_2. D.W. and J.E.G. provided the bulk FGT crystals. J.L. and J.H.E. provided the bulk h-BN crystals. All authors contributed to writing the manuscript.

Competing interests

The authors declare no competing interests.

Additional information

Supplementary information The online version contains supplementary material available at https://doi.org/10.1038/s41563-022-01275-5.

Correspondence and requests for materials should be addressed to Simranjeet Singh.

Peer review information *Nature Materials* thanks Saroj Dash and the other, anonymous, reviewer(s) for their contribution to the peer review of this work.

Reprints and permissions information is available at www.nature.com/reprints.